Frequency Scanning Interferometry Multi-Channel Synchronous Ranging Based on Rapid Suppression of Doppler Error

Qiang Zhou, Tengfei Wu, Xinyue Long, Zhoumo Zeng, *Member, IEEE*, and Jigui Zhu

***Abstract*—Multi-channel synchronous distance measurement is of great significance for the structural network monitoring of large-scale equipment manufacturing. The precision, efficiency, flexibility of measurement directly impacts the operation quality in manufacturing. In this paper, we propose a multi-channel synchronous rapid absolute distance measurement (ADM) system based on frequency scanning interferometry (FSI). A dual-interferometer structure was presented, by introducing optical intensity splitting inside the measurement interferometer to expand channels, reducing the multi-channel system complexity and ensuring the unity of the traceability chain. The system employs dual-laser interferometric signals mixing after spectral segmentation to achieve rapid suppression of Doppler error during the transmission of optical signal, significantly avoiding complex digital signal processing time for interference-signal overlap and improving the efficiency. To validate the performance of the system, we have employed a simulation to verify the target distance extraction of 10 channels. Subsequently, we conducted distance measurement experiments in different vibration conditions utilizing retroreflectors as the targets. The experimental results demonstrate that the Doppler effect has been significantly suppressed, and the precision of the stationary target reaches 1 μm particularly, indicating that this system has high potential in application for high-precision structural monitoring.**

***Index Terms*—Absolute distance measurement, dynamic error, frequency scanning interferometry, multi-channel.**

I. Introduction

With the development of high-end manufacturing, the structural monitoring of large-scale assembly systems plays a crucial role in ensuring their long-term stable operation [1], [2]. Large scientific projects, such as large-diameter optical telescopes, particle accelerators, and spacecraft, are composed of numerous components that exhibit strong correlations between them [3], [4], [5]. During the assembly, operation, and regular calibration of these systems, it is essential to synchronously measure the position changes of a large number of nodes in the structural network to obtain the attitude or deformation information of each component, thereby ensuring the service quality of the equipment. Precision length measurement [6], [7], [8], as a fundamental issue of spatial coordinate measurement, has generated new requirements for network structure monitoring tasks in large-scale multi-component assembly systems, requiring a high-precision, easily expandable, and flexible multi-channel synchronous length measurement method.

Laser interferometry, with its advantages of range, accuracy, and flexibility, has been widely used in the field of precision length measurement [9], [10]. On the basis of mature single-channel laser length measurement technology, various multi-channel synchronous length measurement methods have been derived. The most classic method is multiple parallel beam laser interferometry for measuring geometric motion deviation, such as the XM-60 of Renishaw [11] and the 10735A of Keysight [12]. However, due to the fixed measurement direction, it is mainly used for the calibration of instruments such as coordinate measuring machines (CMM) and precision machine tools. The emergence of multi-length intersection methods [13], [14] represented by the Laser Tracer system [14] has improved the spatial flexibility of length measurement. This method consists of multiple single-channel length measurement systems combined in space, and through multi-station length observations of the same target point, it forms the basic form of multi-channel synchronous length measurement, which can obtain higher point accuracy. However, due to the complexity of single-channel length measurement systems, the contradiction between the number of channels and the standard unification, the expandability of this method is poor. In recent years, new length measurement methods such as frequency scanning interferometry [15], [16], [17] and femtosecond optical frequency comb interferometry [18], [19] have been continuously developed, and they have the ability of on-site high-precision absolute distance measurement (ADM). The derived multi-length synchronous constraint is no longer confined to specific structural forms, and the channel expansion is more flexible. They directly process optical signal and realize multi-channel synchronous length measurement based on optical signal splitting. According to different splitting methods, the implementation of channel expansion also varies, such as expanding channels according to frequency bands using optical frequency splitting method [20], according to diffraction

Manuscript received 28 November 2023; revised 22 January 2024; accepted 12 May 2024. Date of publication 15 May 2024; date of current version 2 September 2024. This work was supported by the National Natural Science Foundation of China under Grant 52127810, Grant 52275539, and Grant 51721003. *(Corresponding author: Tengfei Wu.)*

The authors are with the State Key Laboratory of Precision Measuring Technology and Instruments, Tianjin University, Tianjin 300072, China (e-mail: zhouqiang0530@tju.edu.cn; wtf@tju.edu.cn; lxy150250@163.com; zhmzeng@tju.edu.cn; jiguizhu@tju.edu.cn).

Color versions of one or more figures in this article are available at https://doi.org/10.1109/JLT.2024.3401585.

Digital Object Identifier 10.1109/JLT.2024.3401585

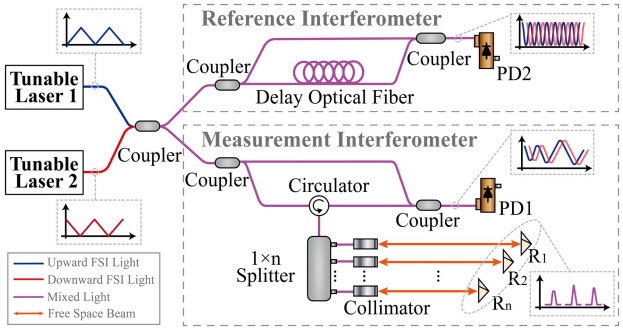

Fig. 1. Schematic of a FSI multi-channel ranging system. PD: photodetector; R: retroreflector.

angles using diffraction principle [21], [22] and according to energy using optical intensity splitting method [11], [23]. Currently, the most feasible and practical solution is using optical intensity splitting to expand the channel, which could well ensure the time synchronization of each channel measurement. The multi-channel ADM technology investigated by John Dale of Oxford University is one of the main representatives [23], and then developed into a commercial instrument, absolute multiline technology system (Multiline System). This system has been tried in the field of mechanical device deformation measurement, and has shown great advantages in expansion capability, flexibility, and measurement accuracy. However, the overall optical path structure of this system reflects that each additional measurement channel requires adding a measurement interferometer, which increases the complexity of the system and makes it difficult to completely unify the standards of each channel. The length extraction accuracy of each channel is easily affected by the Doppler effect [6], [23], [24] caused by target vibration, and two tunable lasers are required to scan the optical frequency in opposite directions to compensate this Doppler error. In this optical path, the interferometric signals of two opposite scans are overlapped together, and the length extraction cannot avoid the separation filtering and phase analysis of these two signals, which is a complex and time-consuming process, limiting the improvement of measurement efficiency and accuracy.

In this paper, a FSI multi-channel synchronous rapid distance measurement system has been proposed. This system employs a dual-interferometer structure, by introducing optical intensity splitting inside the measurement interferometer to expand the measurement channel, which reduces the complexity of the optical path and ensures the unity of the traceability chain for multiple measurements. Then, the Doppler effect in FSI is suppressed by opposite scanning frequency method using two frequency-tunable lasers, and the interference-signal overlap is solved by an optimization method based on interference-signal mixing after spectral separation. Furthermore, the full width at half maximum (FWHM) of spectral peak is used to distinguish multi-channel targets and pseudo peaks generated by signal mixing. This method achieves error compensation for Doppler effect during optical signal transmission, which reduces a large amount of signal processing time, improves the efficiency of length measurement, and avoids errors caused by algorithms. The paper is organized as follows. In Section II, the basic FSI multi-channel synchronous measurement mathematical model was established, and the Doppler effect caused by target vibration in FSI technology was analyzed. Then, a rapid suppression method for the Doppler effect based on opposite-scanning interference-signal mixing technique was proposed. In Section III, the performance of the system was evaluated through experiments under different vibration conditions, particularly for stationary targets, with a repeatability precision of approximately 1 μm. Finally, the conclusion and discussion are summarized in Section IV.

II. Principle and Method

A. FSI Multi-Channel Ranging Model

A multi-channel FSI ranging model was proposed as shown in Fig. 1, in which a 1×n intensity splitter is introduced inside the measurement interferometer to expand the measurement channel, directly emitting light to multiple retroreflectors through collimators. The use of 1×n intensity splitter could effectively maintain real-time measurement across multiple channels, avoiding the issue of multi-channel asynchronous observation when using wavelength division multiplexing (WDM) in FSI. Besides, the differential method [6], [23], using two tunable lasers with opposite optical frequency scanning directions, is utilized to address the Doppler effect, which could achieve a unique compensation precision. In our model, all channels share one optical path and one detection device, so the complexity of multi-channel expansion has been significantly reduced, and the error traceability chain of different channel has been unified. The interferometric signal of measurement interferometer $I_{\mathrm{m,mul}}(t)$ detected by PD1 could be represented as

$$\begin{aligned} I_{\mathrm{m,mul}}(t) &= \sum_{\mathrm{i}=1}^{n} I_{\mathrm{m,i,u}}(t) + \sum_{\mathrm{i}=1}^{n} I_{\mathrm{m,i,d}}(t) \\ &= \sum_{\mathrm{i}=1}^{n} A_{\mathrm{m,i,u}} \cos\left[\phi_{\mathrm{m,i,u}}(t)\right] + \sum_{\mathrm{i}=1}^{n} A_{\mathrm{m,i,d}} \cos\left[\phi_{\mathrm{m,i,d}}(t)\right], \end{aligned} \tag{1}$$

where $I_{\mathrm{m,i,u}}(t)$, $I_{\mathrm{m,i,d}}(t)$ are the interferometric signals of each retroreflector i, wherein u represents upward-scanning signal, d represents downward-scanning signal. $A_{\mathrm{m,i,u/d}}(t)$ represents the signal amplitude, and $\phi_{\mathrm{m,i,u/d}}(t)$ is the signal phase. Each sub interferometric signal exhibits periodic change during laser frequency scanning, and the phase $\phi_{\mathrm{m,i,u/d}}$ of each sub-signal could be expressed as

$$\begin{aligned} \phi_{\mathrm{m,i,u/d}} \approx \frac{2\pi}{c} \cdot \left[D_{\mathrm{m,i,t_0}} \cdot \Delta\nu_{\mathrm{u/d}}(t) + \Delta D_{\mathrm{m,i}}(t) \cdot \nu_{\mathrm{u/d,t_0}}\right] \\ + \phi_{\mathrm{m,i,u/d,t_0}}, \end{aligned} \tag{2}$$

where c is the speed of light, $D_{\mathrm{m,i,t0}}$ is the initial absolute distance at scanning start point, $\triangle D_{\mathrm{m,i}}(t)$ represents the distance variation in a scanning cycle, $\triangle\nu_{\mathrm{u/d}}(t)$ is the optical frequency change of laser, $\nu_{\mathrm{u/d,t0}}$ represents the initial scanning frequency

of laser, the instantaneous laser frequency is $\nu(t) = \nu_{\mathrm{u/d,t0}} + \triangle\nu_{\mathrm{u/d}}(t)$, and $\phi_{\mathrm{m,i,u/d,t0}}$ is the initial phase.

The measurement accuracy of distance $D_{\mathrm{m,i,t0}}$ usually depends on the accuracy of optical frequency change $\triangle\nu_{\mathrm{u/d}}(t)$. In practice, although the laser exhibits linear scanning, nonlinear fluctuations in optical frequency would still occur. Generally, introducing a reference interferometer enables continuous monitoring of optical frequency changes with high accuracy and resolution as shown in Fig. 1. In the reference interferometer, a delay optical fiber is used to generate reference OPD D_{r}. Similarly, the phase $\phi_{\mathrm{r,u/d}}$ of interferometric signal could be expressed as

$$\phi_{\mathrm{r,u/d}}=\frac{2\pi}{c}\cdot D_{\mathrm{r}}\cdot\Delta\nu_{\mathrm{u/d}}\left(t\right)+\phi_{\mathrm{r,u/d,t_0}}. \tag{3}$$

Therefore, the change of optical frequency $\triangle\nu_{\mathrm{u/d}}(t)$ could be obtained by (3). Then, by substituting this frequency change into the corresponding measurement interferometric signal, the initial distance at scanning start point $D_{\mathrm{m,i,t0}}$ could be obtained by

$$D_{\mathrm{m,i,t_0}}=\frac{\Delta\phi_{\mathrm{m,i,u/d}}\left(t\right)}{\Delta\phi_{\mathrm{r,u/d}}\left(t\right)}D_{\mathrm{r}}-\frac{\nu_{\mathrm{u/d,t_0}}}{\Delta\nu_{\mathrm{u/d}}\left(t\right)}\Delta D_{\mathrm{m,i}}\left(t\right). \tag{4}$$

It could be seen that the first term contains correct distance information and the second term is an additional error arising from the distance variation $\triangle D_{\mathrm{m,i}}(t)$. The factor $\nu_{\mathrm{u/d,t0}}/\triangle\nu_{\mathrm{u/d}}(t)$ usually ranges from several hundreds to thousands under different scanning range, which is the Doppler effect. This error has a magnified effect and is more severe during measurement at the manufacturing site. Here, we present simulations of Doppler effect under different uniform drift (UD) mode and harmonic vibration (HV) mode, as depicted in Fig. 2. To compensate for this error, four interferometric phases generated by the two frequency-tunable lasers and two interferometers have been used to obtain the distance $D_{\mathrm{m,i,t0}}$ without Doppler effect

$$D_{\mathrm{m,i,t_0}}=\frac{\Delta\phi_{\mathrm{m,i,d}}\left(t\right)\cdot\nu_{\mathrm{u,t_0}}-\Delta\phi_{\mathrm{m,i,u}}\left(t\right)\cdot\nu_{\mathrm{d,t_0}}}{\Delta\phi_{\mathrm{r,d}}\left(t\right)\cdot\nu_{\mathrm{u,t_0}}-\Delta\phi_{\mathrm{r,u}}\left(t\right)\cdot\nu_{\mathrm{d,t_0}}}D_{\mathrm{r}}, \tag{5}$$

where $\triangle\phi_{\mathrm{m/r,i/,d/u}}$ is the phase change in measurement interferometer or reference interferometer. Furthermore, the $D_{\mathrm{m,i,t0}}$ could also be determined by the linear regression or frequency-resampling method [25].

B. Rapid Suppression Method for the Doppler Effect

It should be noted that the distance calculation cannot be separated from the procedure of Doppler effect compensation. However, from (1), when a single-channel measurement is conducted, the interferometric signal of measurement interferometer is overlapped together by two signals: upward scanning $I_{\mathrm{m,1,u}}$(t) and downward scanning $I_{\mathrm{m,1,d}}$(t). To complete the distance calculation shown in (5), four phase changes $\triangle\phi_{\mathrm{m,1,u}}$, $\triangle\phi_{\mathrm{m,1,d}}$, $\triangle\phi_{\mathrm{r,u}}$, and $\triangle\phi_{\mathrm{r,d}}$ need to be extracted from the superimposed signals. Usually, this process requires filtering of frequency domain information to complete the separation of superimposed signals. For example, first, the superimposed signals are sequentially subjected to Fourier transform, spectral windowing function filtering, and inverse Fourier transform to achieve signal separation. Then, the separated signals are subjected to Hilbert transform to obtain the four phase information mentioned above, and a point-by-point phase calculation is necessary to compensate Doppler error according to (5). Obviously, this long computer-dependent digital signal processing process has a certain loss in measurement efficiency and accuracy. Therefore, we focus on completing the above signal processing during signal transmission process, also before interferometric signal acquisition, which will improve measurement efficiency significantly and avoid errors caused by the algorithm.

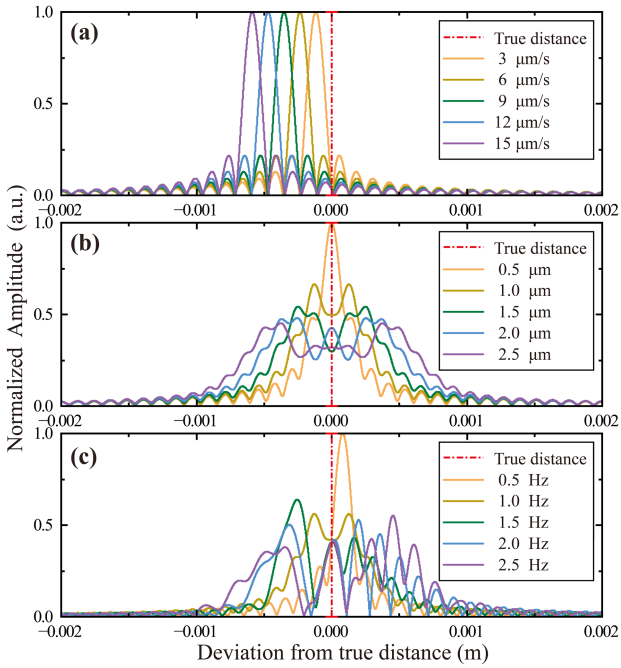

Fig. 2. Simulations of Doppler effect in different conditions. These conditions include: (a) Uniform drift (UD) at different velocities; (b) Harmonic vibration (HV) at different vibration amplitudes; and (c) Harmonic vibration (HV) at different vibration frequencies.

We use spectral segmentation method for signal separation and signal mixing method to achieve Doppler error suppression during signal transmission. As illustrated in Fig. 3, the WDMs are introduced to separate the upward and downward scanning signals based on the spectral range, and the Doppler effect is rapidly suppressed by mixers. In the dual interferometers, the acousto-optical modulators are used for frequency shifting. In this scheme, the interferometric phases generated by two lasers in reference interferometer could be expressed by

$$\phi'_{\mathrm{r,u}}\left(t\right)=2\pi\left[\frac{D_{\mathrm{r}}\cdot\Delta\nu_{\mathrm{u}}\left(t\right)}{c}+f_{AOM1}\cdot t\right]+\phi_{\mathrm{r,u,}t_0}, \tag{6}$$

$$\phi'_{\mathrm{r,d}}\left(t\right)=2\pi\left[\frac{D_{\mathrm{r}}\cdot\Delta\nu_{\mathrm{d}}\left(t\right)}{c}+f_{AOM1}\cdot t\right]+\phi_{\mathrm{r,d,}t_0}, \tag{7}$$

where ϕ'$_{\mathrm{r,u}}$ and ϕ'$_{\mathrm{r,d}}$ represent the interferometric phases of the upward and downward scanning lasers, respectively. f_{AOM1} denotes the frequency shift of AOM1, while $\triangle\nu_{\mathrm{u}}(t)$ and $\triangle\nu_{\mathrm{d}}(t)$ represent the frequency changes of the two lasers. It should be

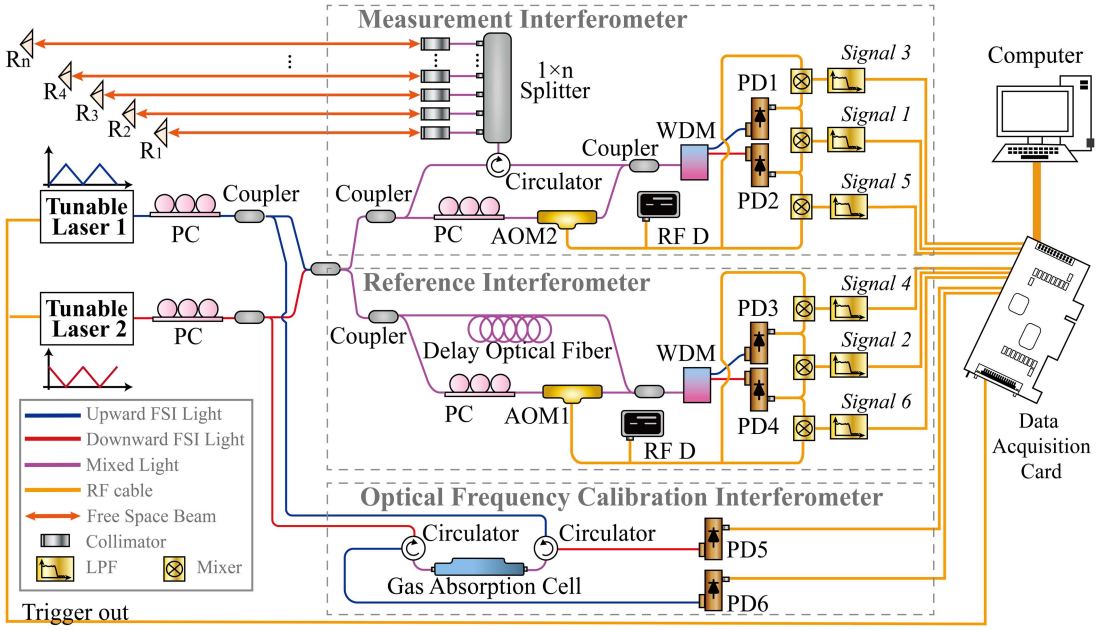

Fig. 3. The multi-channel synchronous rapid FSI system for parallel measurement. PC: Polarization controller; AOM: Acousto-optical modulator; RFD: Radio-frequency Driver; WDM: Wavelength division multiplexer; LPF: Low-passed filter.

noted that $\triangle\nu_{\mathrm{d}}(t)$ is negative value due to the gradual decrease in optical frequency.

Correspondingly, the interferometric phases $\phi'_{\mathrm{m},1,\mathrm{u}}$ and $\phi'_{\mathrm{m},1,\mathrm{d}}$ generated by the upward scanning and downward scanning lasers could be expressed in

$$\phi'_{\mathrm{m},1,\mathrm{u}}(t) \approx \frac{2\pi}{c}\left[D_{\mathrm{m},1,\mathrm{t_0}}\cdot\Delta\nu_{\mathrm{u}}(t)+\Delta D_{\mathrm{m},1}(t)\cdot\nu_{\mathrm{u,t_0}}\right] + 2\pi f_{AOM2}\cdot t+\phi_{\mathrm{m},1,\mathrm{u},t_0}, \tag{8}$$

$$\phi'_{\mathrm{m},1,\mathrm{d}}(t) \approx \frac{2\pi}{c}\left[D_{\mathrm{m},1,\mathrm{t_0}}\cdot\Delta\nu_{\mathrm{d}}(t)+\Delta D_{\mathrm{m},1}(t)\cdot\nu_{\mathrm{d,t_0}}\right] + 2\pi f_{AOM2}\cdot t+\phi_{\mathrm{m},1,\mathrm{d},t_0}. \tag{9}$$

Then, two WDMs are used to separate the interferometric signals of upward scanning and downward scanning based on the spectral range, and two mixers are used here to obtain the product of two opposite scanning interferometric signals, respectively. The signals passing through the mixer could be expressed in

$$\begin{aligned} I_{\mathrm{r,mixer}}(t) &= I_{\mathrm{r,u}}(t)\cdot I_{\mathrm{r,d}}(t)\\ &= I_{\mathrm{r0}}\cdot\cos\left[\phi'_{\mathrm{r,u}}(t)\right]\cdot\cos\left[\phi'_{\mathrm{r,d}}(t)\right]\\ &= \frac{I_{\mathrm{r0}}}{2}\left\{\cos\left[\phi'_{\mathrm{r,u}}(t)-\phi'_{\mathrm{r,d}}(t)\right]\right.\\ &\quad\left.+\cos\left[\phi'_{\mathrm{r,u}}(t)+\phi'_{\mathrm{r,d}}(t)\right]\right\}, \end{aligned} \tag{10}$$

$$\begin{aligned} I_{\mathrm{m,1,mixer}}(t) &= I_{\mathrm{m,1,u}}(t)\cdot I_{\mathrm{m,1,d}}(t)\\ &= I_{\mathrm{m0}}\cdot\cos\left[\phi'_{\mathrm{m,1,u}}(t)\right]\cdot\cos\left[\phi'_{\mathrm{m,1,d}}(t)\right]\\ &= \frac{I_{\mathrm{m0}}}{2}\left\{\cos\left[\phi'_{\mathrm{m,1,u}}(t)-\phi'_{\mathrm{m,1,d}}(t)\right]\right.\\ &\quad\left.+\cos\left[\phi'_{\mathrm{m,1,u}}(t)+\phi'_{\mathrm{m,1.d}}(t)\right]\right\}. \end{aligned} \tag{11}$$

A sum–frequency signal and a difference–frequency signal, expressed as the output signals of the mixers, are shown in (10) and (11). Consequently, the difference–frequency signal could be obtained by using a low-passed filter, as shown in

$$\begin{aligned} I_{\mathrm{r},LFP} &= \cos\left[\phi'_{\mathrm{r,u}}(t)-\phi'_{\mathrm{r,d}}(t)\right]\\ &= \cos\left[\frac{2\pi\cdot D_r}{c}\cdot\left(\Delta\nu_{\mathrm{u}}(t)-\Delta\nu_{\mathrm{d}}(t)\right)\right], \end{aligned} \tag{12}$$

$$\begin{aligned} I_{\mathrm{m},1,LFP} &= \cos\left[\phi'_{\mathrm{m,1,u}}(t)-\phi'_{\mathrm{m,1,d}}(t)\right]\\ &= \cos\left[\frac{2\pi\cdot D_{\mathrm{m},1,\mathrm{t_0}}}{c}\cdot\left(\Delta\nu_{\mathrm{u}}(t)-\Delta\nu_{\mathrm{d}}(t)\right)\right.\\ &\quad\left.+2\pi\cdot\left(\nu_{\mathrm{u,t_0}}-\nu_{\mathrm{d,t_0}}\right)\cdot\frac{\Delta D_{\mathrm{m},1}(t)}{c}\right]. \end{aligned} \tag{13}$$

Extracting the optical frequency variation from (12) and substituting it into (13) can obtain a complete mathematical model of the measured distance

$$\begin{aligned} D_{\mathrm{m},1,\mathrm{t_0}} &= \frac{\Delta\phi_{\mathrm{m},1,LFP}(t)}{\Delta\phi_{\mathrm{r},LFP}(t)}\cdot D_{\mathrm{r}}-\frac{\nu_{\mathrm{u,t_0}}-\nu_{\mathrm{d,t_0}}}{\Delta\nu_{\mathrm{u}}(t)-\Delta\nu_{\mathrm{d}}(t)}\\ &\quad\cdot\Delta D_{\mathrm{m},1}(t), \end{aligned} \tag{14}$$

where $\triangle\phi_{\mathrm{r},LEP}$ and $\triangle\phi_{\mathrm{m},1,LEP}$ are the phase changes of $I_{\mathrm{r},LEP}$ and $I_{\mathrm{m},1,LEP}$, respectively.

Comparing between (14) and (4), it is evident that complete elimination of the Doppler error could be achieved when the initial frequency of upward scanning $\nu_{\mathrm{u,t0}}$ is equal to that of downward scanning $\nu_{\mathrm{d,t0}}$. Furthermore, even if the two initial frequencies are not ideally equal, the Doppler effect could still be effectively suppressed, as $(\nu_{\mathrm{u,t0}}-\nu_{\mathrm{d,t0}})$ is generally more than a hundred times smaller than $(\Delta\nu_{\mathrm{u}}(t)-\Delta\nu_{\mathrm{d}}(t))$, so the coefficient of the second term in (14) is much smaller than 1. Neglecting

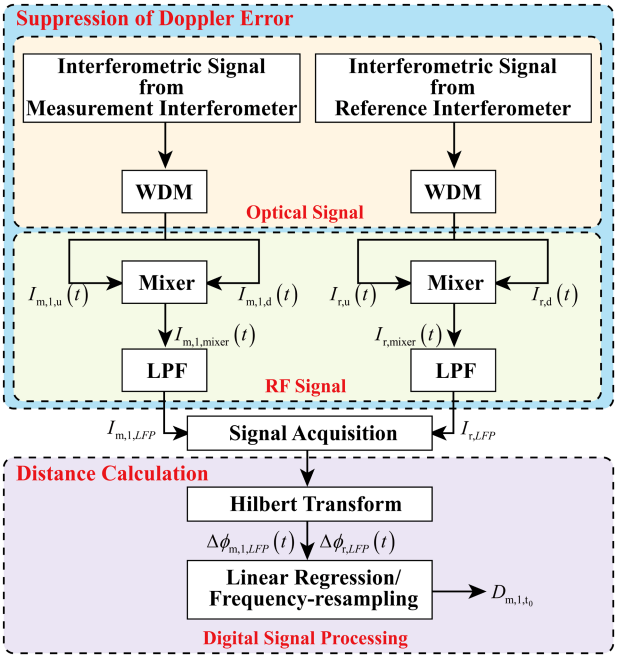

Fig. 4. Overall procedure of interferometric signal processing.

this residual error, the ADM at the initial time of laser scanning after suppressing Doppler effect could be rapidly obtained.

In this system, signal 1 and signal 2 are used for rapid suppression of Doppler error, while signal 3, signal 4, signal 5, and signal 6 are used for comparison without suppressing the Doppler effect. The overall procedure of signal processing is shown in Fig. 4. The signal processing during signal transmission before interferometric signal acquisition is mainly used to suppress the Doppler error, and the digital signal processing algorithm after signal acquisition is mainly used to calculate the distance of the signals after suppressing the Doppler error, including extracting phase using Hilbert Transform, eliminating scanning nonlinear errors in laser using linear regression or frequency-resampling methods [25], and finally obtaining the measured distance.

C. Multi-Channel Targets Distinction Strategy

After solving the overlap issue between the upward scanning signal and downward scanning signal, in this section, we discuss the distinction strategy of multiple target superposition. Since the signal mixing can be regard as calculating the multiplication of two signals, when faced with multi-channel ranging, the signal mixing method will generate pseudo spectrum peaks. It is necessary to distinguish between real targets and pseudo spectrum peaks among numerous frequency components. By using a 1×n splitter to expand channels, every channel will generate an interferometric signal of upward scanning and an interferometric signal of downward scanning. After spectral segmentation, the signals generated by the same laser will be superimposed and detected by one photodetector.

Then, compared with (11), the mixed signal after mixer could be rewritten as

$$I_{\mathrm{m,mul,mixer}}(t) = I_{\mathrm{m,mul,u}}(t) \cdot I_{\mathrm{m,mul,d}}(t)$$

$$\begin{aligned}
&= I_{\mathrm{m0}} \cdot \left\{\cos\left[\phi'_{\mathrm{m,1,u}}(t)\right] + \cos\left[\phi'_{\mathrm{m,2,u}}(t)\right] + \cdots \right. \\
&\quad \left. + \cos\left[\phi'_{\mathrm{m,n,u}}(t)\right]\right\} \cdot \\
&\quad \left\{\cos\left[\phi'_{\mathrm{m,1,d}}(t)\right] + \cos\left[\phi'_{\mathrm{m,2,d}}(t)\right] + \cdots \right. \\
&\quad \left. + \cos\left[\phi'_{\mathrm{m,n,d}}(t)\right]\right\} \\
&= I_{\mathrm{m0}} \cdot \sum_{\mathrm{i=1,j=1}}^{\mathrm{i=n,j=n}} \left\{\cos\left[\phi'_{\mathrm{m,i,u}}(t)\right] \cdot \cos\left[\phi'_{\mathrm{m,j,d}}(t)\right]\right\} \\
&= \frac{I_{\mathrm{m0}}}{2} \cdot \sum_{\mathrm{i=1,j=1}}^{\mathrm{i=n,j=n}} \left\{\cos\left[\phi'_{\mathrm{m,i,u}}(t) - \phi'_{\mathrm{m,j,d}}(t)\right] \right. \\
&\quad \left. + \cos\left[\phi'_{\mathrm{m,i,u}}(t) + \phi'_{\mathrm{m,j,d}}(t)\right]\right\}, \qquad (15)
\end{aligned}$$

where n is the number of the channel. After being filtered by a LPF, (13) could be rewritten as

$$\begin{aligned}
I_{\mathrm{m,mul},LFP}(t) &\approx \sum_{\substack{\mathrm{i=1,j=1} \\ \mathrm{i\neq j}}}^{\mathrm{i=n,j=n}} \cos\left[\phi'_{\mathrm{m,i,u}}(t) - \phi'_{\mathrm{m,j,d}}(t)\right] \\
&+ \sum_{\mathrm{i=j=1}}^{\mathrm{n}} \cos\left\{\frac{2\pi \cdot D_{\mathrm{m,i,t_0}} \cdot \left[\Delta\nu_{\mathrm{u}}(t) - \Delta\nu_{\mathrm{d}}(t)\right]}{c}\right. \\
&\left. + 2\pi \cdot \left(\nu_{\mathrm{u,t_0}} - \nu_{\mathrm{d,t_0}}\right) \frac{\Delta D_{\mathrm{m,i}}(t)}{c}\right\}. \qquad (16)
\end{aligned}$$

It can be seen that the low-pass filtered signal will generate *[n+(n-1)×n]* frequency components. The second term in (16) contains the distance information of multi-channel targets after suppressing the Doppler effect, which is similar with (13). The first term, however, represents an incorrect combination of signals from different targets. Due to the fact that the signal frequency in the first term is not unstable, its spectrum would broaden upon the Fourier transform. On the contrary, the frequency of the signal in the second term is stable. Therefore, the FWHM of spectral peaks could be utilized to effectively distinguish between genuine multi-channel targets and pseudo peaks generated by mixing.

Then, (12) is used as a sampling clock to eliminating the impact of laser scanning nonlinearity, yielding (17)

$$2\pi\left(\frac{D_r \cdot \Delta\nu_{\mathrm{u}}(t)}{c} - \frac{D_r \cdot \Delta\nu_{\mathrm{d}}(t)}{c}\right) = 2\pi k \qquad (17)$$

where k is the frequency sampling point index. Usually, the length of the delay optical fiber should be set to 4 times or more of the measurement range in order to meet the Nyquist sampling theorem. With (17) and (16), the resampled signal (measurement interferometric signal after correcting the scanning non-linearity) can be expressed as

$$I_{\mathrm{m,mul,re}}(k) \approx \sum_{\mathrm{i=1}}^{\mathrm{n}} \cos\left[2\pi \cdot \frac{D_{\mathrm{m,i,t_0}}}{D_r} k\right] + \sum \cos\phi_{error}. \qquad (18)$$

In conclusion, the application of Fast Fourier transforms and frequency domain filtering on (18) yields distance spectrums of targets, including some pseudo peaks generated by the cross

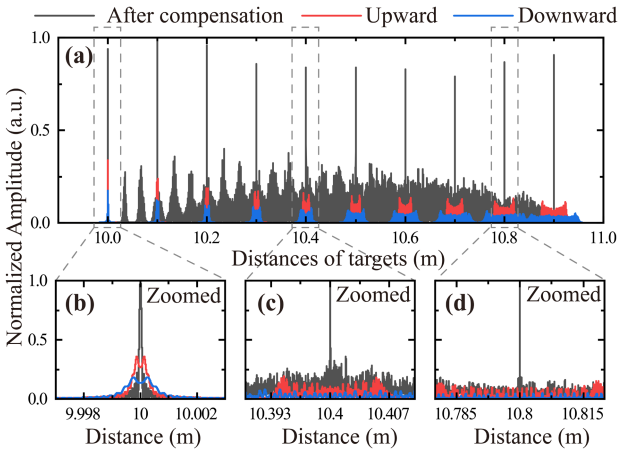

Fig. 5. Simulation of multi-channel targets. (a) The distance spectrum of 10 targets. (b) Target at 10.0 m. (c) Target at 10.4 m. (d) Target at 10.8 m.

combination of different targets. Besides, in our method, the efficiency of obtaining multi-target spectrum is the same as that of obtaining a single target, which means that when conducting multi-target measurements, the measurement speed does not decrease with the increase of the target. It is worth noting that the distinction between real target distances relies on prior information. Usually, in large-scale equipment structure monitoring tasks, the distance variation of each channel is relatively small, so our method also meets this requirement.

To verify the feasibility of the distinguishing method, a simulation of 10 targets is conducted, as depicted in Fig. 5. These targets are measured from 10.0 m to 10.9 m with 0.1 m interval and undergo harmonic vibrations. The vibration amplitudes are set from 1 μm to 10 μm with 1 μm interval, and the vibration frequencies are set from 1 Hz to 10 Hz with 1 Hz interval, respectively. After suppressing the Doppler effect (black), the spectrum of each target is evidently narrower than that before compensation (red and blue), and two pseudo peaks would be generated between every two real peaks. Because the scanning range of the downward scanning (blue) is larger than that of the upward scanning (red), the spectrum broadening is more severe. The FWHM of the pseudo peak is wider than the real peak, facilitating their distinction. Notably, while the FWHM enables differentiation between real and pseudo peaks, the approximate separation between each real peaks needs to be roughly known in advance. For example, we could obtain prior distances of all channels by implementing measurements for each channel one by one, and then use the synchronous measurement method provided above to monitor the distance changes of each measurement channel.

III. Experiments and Results

In this section, in order to verify the performance of the above system and method, some experiments were carried out under different conditions.

A. Experimental Configuration and Data Analysis

The experimental setup depicted in Fig. 3 was constructed using two identical external cavity lasers (81606A #116 series, Keysight) capable of providing a mode-hop-free tuning range of 1490 nm to 1640 nm and a tuning speed of up to 200 nm/s. Tunable laser 1 was swept from 1545 nm to 1535 nm at a rate of 20 nm/s, while tunable laser 2 was swept from 1547 nm to 1567 nm at a rate of 40 nm/s, resulting in a scan time of approximately 0.5 s. It is noteworthy that there is no requirement for the sweep speed of the two lasers, and they could also be set to the same speed in our system. Following polarization state adjustment, the light from both lasers was combined using a fiber coupler and directed into the measurement interferometer and reference interferometer, respectively. The two interferometers are designed in the form of fiber Mach-Zender interferometers. The key difference between them lies in the origin of the optical path difference (OPD): the measurement interferometer generates OPD through targets located in free space, while the reference interferometer generates OPD through a long delay fiber of approximately 110 m. Acousto-optical modulators are utilized to generate frequency shifts. Specifically, the T-M080-0.4C2J-3-F2S model from Gooch & Housego generates a frequency shift of 80 MHz in the measurement interferometer, while the MT110-IIR20-FIO-PM0.5-J1-A model from AA Opto-electronic generates a frequency shift of 110 MHz in the reference interferometer. Similarly, the polarization controllers are used to adjust the polarization state of the light passing through the AOM branch to maximize the interferometric signal intensity. Then, the WDMs (port1: 1529.4-1545 nm, port2: 1547-1570 nm) are introduced to separate interferometric signals from two frequency-tunable lasers in two interferometers, the blue line represents the signal of laser 1, while the red represents laser 2. These four interferometric signals are detected by photodetectors PD1, PD2, PD3, and PD4 (PDB470C, Thorlabs), respectively. The signals from PD1 and PD2 are mixed together at a mixer, filtered by a low passed filter, and then the measurement interferometric signal after suppressing Doppler effect could be acquired, which is called Signal1. By mixing the signal of PD1 and the local oscillator signal of AOM1, the measurement interferometric signal (upward scanning) without suppressing could be acquired after removing the high frequency components, which is called Signal3. The measurement interferometric signal (downward scanning) could also be acquired and expressed as Signal5. Similarly, the reference interferometric signals, Signal2, Signal4, and Signal6, were acquired using the same method. The bandwidth of the all LPFs (SLP-27+, Mini-Circuits) is DC to 27 MHz. To separate the upward scanning light and downward light in the optical frequency calibration interferometer, two circulators were introduced, and the gas absorption signals were detected by PD5 and PD6 (PDB450C, Thorlabs). All signals were digitized and recorded by a digital acquisition system (PXIe-5160, National Instruments) at a sampling rate of 20 MS/s, and further processing was performed on a computer.

The synchronization control of two tunable lasers is shown in the Fig. 6(a). An arbitrary waveform generator (DG5102, RIGOL) controlled by computer was used to generate two synchronous pulses, which could provide dual-channel signals with a maximum frequency of 100 MHz and trigger lasers from the trigger in ports. When the laser starts scanning, laser 2 generates a pulse at the trigger output port, which is used to trigger the digital acquisition system to record all the signals. The

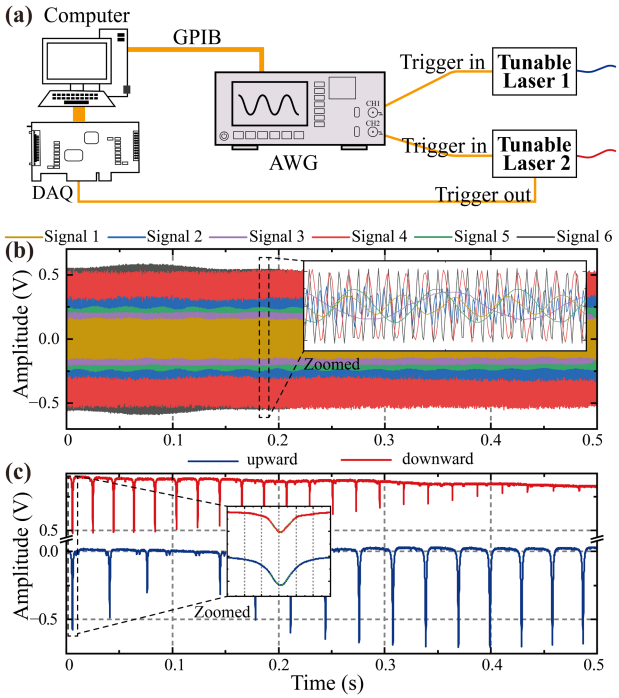

Fig. 6. (a) Dual-laser synchronous control device. (b) Original data of interferometric Signal1 ∼ Signal6. (c) Signal of gas absorption cell. AWG: Arbitrary Waveform Generator.

original interferometric signals in a scanning cycle are shown in Fig. 6(b), and the gas absorption signals are shown in Fig. 6(c). In the experiment, we could observe the synchronization degree of two lasers through the gas absorption signal. The relative time interval between the first peaks of two signals would fluctuate due to the degree of synchronization, which is less than 0.01 s. This error causes a difference in the scanning initial optical frequency ($\nu_{\mathrm{u,t0}} - \nu_{\mathrm{d,t0}}$) approximately 0.2 nm. According to (14), the second error term is much smaller than the actual target vibration, which can be neglected. The fiber tail length of WDMs is basically the same, and the response time difference of PDs could be neglected.

Then, the data processing of digitized signals was shown in Fig. 7. Taking a dynamic target located at 9.77 m with 10 Hz vibration frequency and 4 μm vibration amplitude as an example, the Hilbert transformation was applied to all the interferometric signals to obtain the instantaneous phases. The unwrapped phases are presented in Fig. 7(a), revealing that the reference phases (Signal2, Signal4, Signal6) significantly exceed the measurement phases (Signal1, Signal3, Signal5) in accordance with the Nyquist's theorem. Subsequently, Fig. 7(b) illustrates the phase linear regression method, which is the first approach for distance extraction. The ratio between the measurement phase and the reference phase $\Delta\phi_{\mathrm{m}}(\mathrm{t})/\Delta\phi_{\mathrm{r}}(\mathrm{t})$ was calculated from the green dashed line, and the slope of fitting is 0.060325. Then, according to (14), the distance can be obtained by multiplying the D_{r}, which can be calibrated by a commercial interferometer. The second method of distance extraction is based on the spectrum analysis such as FFT and CZT algorithms, as shown in Fig. 7(c). The distance spectrum

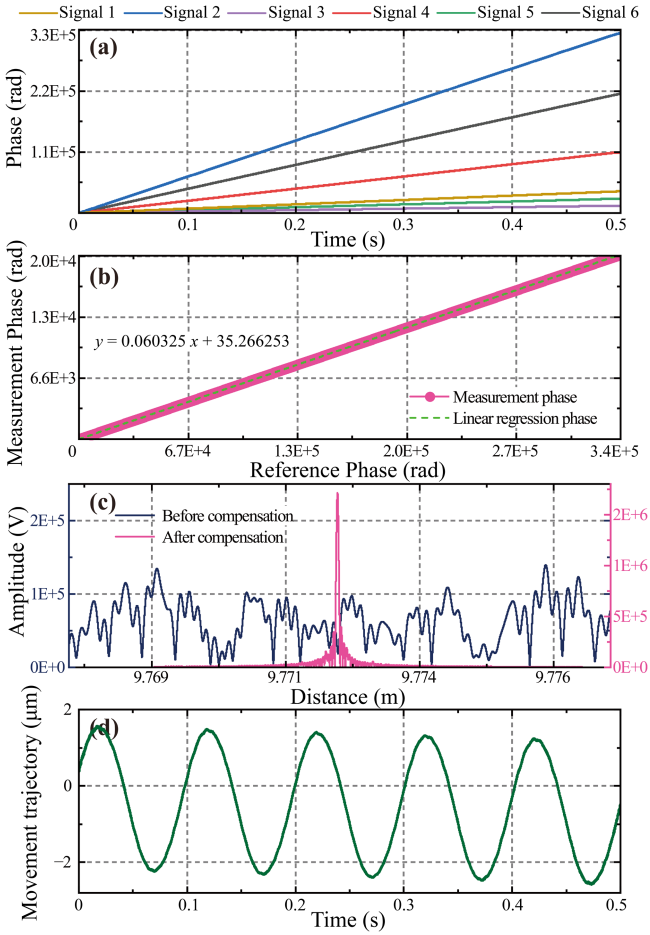

Fig. 7. Procedure of the distance extraction. (a) The unwrapped phases of interferometric signals. (b) Linear regression of the measurement phase and reference phase. (c) The distance spectrum before and after compensation. (d) The movement trajectory of target.

before compensation (black line) was broadened and could not be extracted a single peak. After compensation, the spectrum (pink line) was significantly narrowed, indicating successful suppressing of the Doppler effect. The movement trajectory of target is illustrated in Fig. 7(d). It could be seen that the vibration frequency is about 10 Hz, amplitude is about 4 μm, and a minimal linear drift exists, which is because that the vibration platform is in open-loop state.

B. System Verification Under Different Conditions

As previously mentioned, variations in optical path difference (OPD) during a scanning period can result in magnified errors and a loss of precision. In this section, we aim to verify the system's performance in terms of its ability of rapid initial ADM. To achieve this, we subjected a single retroreflector in free space to various types of motion.

The experimental setup was established on a vibration isolated optical table as shown in Fig. 8(a) . A retroreflector was affixed to a piezo-driven linear positioner (P-622.1CD, Physik Instrumente) capable of providing 250 μm displacement with a resolution of approximately 1 nm. The direction of the free

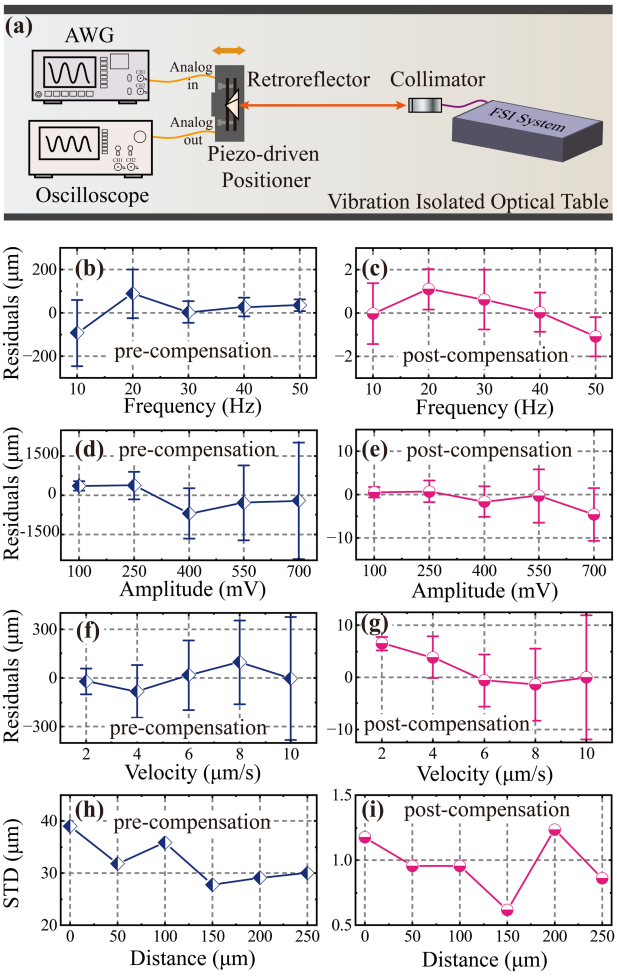

Fig. 8. System verification under different vibration conditions. (a) Experimental setup, (b) and (c) experimental results of harmonic vibration (HV) with different frequencies, (d) and (e) experimental results of harmonic vibration (HV) with different amplitudes, (f) and (g) experimental results of uniform drift (UD) with different velocities, (h) and (i) experimental results of stationary target with different positions.

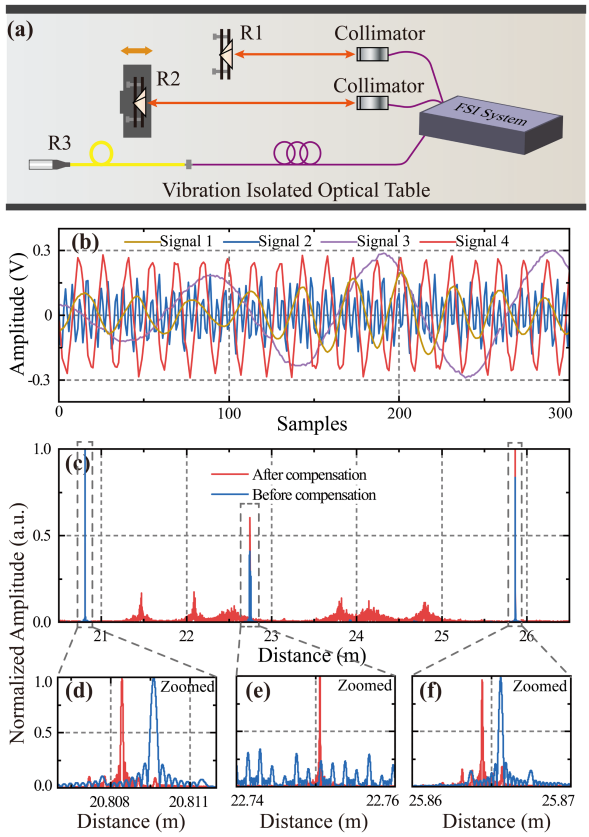

Fig. 9. System verification of multi-channel measurement. (a) Experimental setup. (b) Original data of interferometric signal 1∼4. (c) The distance spectrum of all targets. (d) The distance spectrum of R1. (e) The distance spectrum of dynamic R2. (f) The distance spectrum of R3.

space beam was parallel to the positioner's movement direction. To generate harmonic vibration (HV) and uniform drift (UD), we employed an arbitrary waveform generator to produce a driving signal that connected to the analog in port of the positioner. By setting different sinusoidal and triangle waves, we could create various motion types. The analog out signal of the piezo-driven stage was utilized to monitor the target's movement state, which was a voltage signal proportional to displacement and displayed on an oscilloscope. We employed an incremental interferometer to calibrate the proportional relationship between the output signal and the target displacement, which was approximately 50 μm/V. To emphasize the pre-compensation and post-compensation changes, we collected the signals after Doppler effect compensation and the signals during upward scanning in all experiments.

The experiments were conducted to verify the precision of initial ADM extraction. The ADM after compensation was obtained from Signal1 and Signal2 using the method described in the previous section, while the initial ADM before compensation for comparison was obtained from Signal3 and Signal4. Previous researches have demonstrated that in industrial scenarios, the motion of dynamic targets could be decomposed into harmonic vibration and uniform drift, with vibration frequencies typically below 50 Hz and amplitudes typically below 50 μm. Therefore,

TABLE I
THE STANDARD DEVIATION UNDER DIFFERENT VIBRATION CONDITIONS

Conditions	STD (μm)		Conditions	STD (μm)	
	Before	After		Before	After
HV, 10Hz	153.7	1.4	UD, 2μm/s	78.4	1.2
HV, 20Hz	112.4	0.9	UD, 4μm/s	1629.6	3.9
HV, 30Hz	50.5	1.4	UD, 6μm/s	2150.4	5.0
HV, 40Hz	42.6	0.9	UD, 8μm/s	2576.3	6.9
HV, 50Hz	27.4	0.9	UD, 10μm/s	3788.8	11.5
HV, 100mV	177.2	1.2	Stationary, 0μm	39.0	1.2
HV, 250mV	523.9	2.5	Stationary, 50μm	31.9	1.0
HV, 400mV	965.9	3.6	Stationary, 100μm	35.8	1.0
HV, 550mV	1432.4	6.2	Stationary, 150μm	27.7	0.6
HV, 700mV	2248.5	6.1	Stationary, 200μm	29.1	1.2
			Stationary, 250μm	30.0	0.9

TABLE II
THE STANDARD DEVIATION OF MULITI-CHANNEL MEASUREMENT UNDER DIFFERENT CONDITIONS

R1 (retroreflector)			R2 (dynamic retroreflector)			R3 (fiber optic retroreflector)		
Conditions	STD (μm)		Conditions	STD (μm)		Conditions	STD (μm)	
	Before	After		Before	After		Before	After
Stationary	26.4	1.8	HV, 10Hz	3446.2	2.1	Stationary	18.5	2.2
Stationary	18.5	1.7	HV, 20Hz	7360.1	1.5	Stationary	14.4	2.0
Stationary	27.0	1.5	HV, 30Hz	5338.3	1.5	Stationary	26.2	1.9
Stationary	28.0	0.7	HV, 40Hz	6376.5	0.8	Stationary	14.8	1.1
Stationary	24.0	1.4	HV, 50Hz	2953.7	1.5	Stationary	14.2	1.6
Stationary	14.6	1.5	HV, 100mV	3747.5	1.6	Stationary	8.2	2.0
Stationary	15.4	0.9	HV, 250mV	6896.0	2.0	Stationary	14.4	1.1
Stationary	26.3	1.3	HV, 400mV	6006.6	3.0	Stationary	22.0	1.2
Stationary	15.4	1.2	HV, 550mV	6816.1	4.1	Stationary	13.2	1.3
Stationary	32.1	1.5	HV, 700mV	7305.2	6.5	Stationary	19.8	1.3
Stationary	31.0	2.0	UD, 2μm/s	95.7	2.2	Stationary	11.9	2.2
Stationary	21.7	1.3	UD, 4μm/s	122.5	3.8	Stationary	25.3	1.7
Stationary	24.9	1.4	UD, 6μm/s	276.9	4.2	Stationary	25.2	1.7
Stationary	20.3	1.4	UD, 8μm/s	304.0	5.6	Stationary	14.7	1.9
Stationary	21.4	1.2	UD, 10μm/s	374.7	7.1	Stationary	20.7	1.3

in the first experiment, the positioner was set to a harmonic vibration with a fixed amplitude of 4 μm and a frequency of 10 Hz to 50 Hz with an interval of 10 Hz. 10 individual measurements were taken at each frequency. Due to the hysteresis effect, the actual vibration amplitude varied across frequencies. By adjusting the AWG signal according to the analog out signal, the vibration amplitude of all experiments could be controlled in 4 μm. The system performance evaluated using the standard deviation (STD) of 10 individual measurements, as shown in Table I and Fig. 8. Before compensation the maximum STD was as large as 153.7 μm, but after compensation, the STD is basically around 1 μm, indicating a good compensation effect.

In the second experiment, the positioner was set to a harmonic vibration with a fixed frequency of 10 Hz and an amplitude ranging from 5 μm to 35 μm with 7.5 μm. As the amplitude increases, the STD also increased due to the greater change in position. However, the improved system significantly reduced the STD at each amplitude by at least 150 times. The positioner was also tested with uniform drift at velocities of 2 μm/s to 10 μm/s, and stationary targets at different positions between 0 μm to 250 μm yielding similar conclusions as shown in Table I and Fig. 8. These sub- experiments demonstrate that the system effectively suppresses the Doppler effect of target and has strong robustness to variation in the measured optical path.

C. Multi-Channel Measurement

After verifying the rapid initial ADM abilities of a single target, the multi-channel target distance extraction experiment was performed in this section to verify the system's performance of multiple targets measurement.

The multi-channel measurement implementation was shown in Fig. 9(a). Due to equipment limitations, we employed only three targets to demonstrate the feasibility of precious system for multi-channel measurement, and this experiment could be still able to verify the multi-channel ranging of our proposed solution. The first target was a stationary retroreflector (HRR201-M01, Thorlabs) fixed to the vibration isolated optical table and located in the free space as a stationary target. The second target was a dynamic retroreflector (HRR201-M01, Thorlabs) attached to the piezo-driven linear positioner. The third target was a stationary fiber optic retroreflector (P5-SMF28ER-P01-1, Thorlabs), which was in the fiber throughout the entire optical path. The three targets represent three types of states. The equivalent OPD of the targets were approximately 20.8 m, 22.7 m, and 25.9 m, respectively. In the experiment, dynamic retroreflector2 was subjected to harmonic vibrations (HV) and uniform drifts (UD) with different parameters, and 10 repeated experiments were conducted under each condition.

The measurement results and STDs are shown in Table II and Fig. 9. The origin interferometric signals before and after compensation were shown in Fig. 9(b). It could be seen that the measurement interferometric signals (after compensation: Signal1; before compensation: Signal3) was no longer single frequency signals, but composite signals superimposed with three distance information. The spectrum base on Chirp-Z algorithm is applied to obtain the distance spectrum of three targets, as shown in Fig. 9(c). The zoom spectrums of each target are revealed in Fig. 9(d)–(f). It illustrates clearly that the distance spectrum (blue line) of dynamic target2 was broadened more severely than stationary targets before compensation. After compensation, the

distance spectrums (red line) became narrower, and two pseudo peaks would generate between every two target distance spectrums. The FWHM of the pseudo peak was widened and easy to distinguish, which was consistent with the simulation result in Fig. 5. It's worth explaining that in our simulation and experimental results, this strategy for distinguishing between real and pseudo peaks is feasible. However, for some extremely special situations, such as the superposition of multiple pseudo-peaks and exceeding the power of the real peak, and several targets with the same distance, we believe that the occurrence probability is low and could be avoided by flexibly deploying target positions. The more detailed results are shown in the Table II. For the two stationary targets, retroreflector1 or retroreflector3, the STD before compensation is in the order of tens of micrometers, but after compensation, the STD decreases to below 2 μm. For retroreflector2, the precision has improved significantly after compensation under different vibration conditions. It is noteworthy that the STD of the harmonic vibrations before compensation is much lower than that of section B, because here the distance is extracted using spectrum method, while phase linear regression method was used uses to extract distance in section B. When the distance spectrum was broadened to the extent that the peak could not be identified, the precision of the spectrum method is much lower than that of the phase linear regression method. In summary, all the experimental results demonstrate that the system is effective for multi-channel distance measurement with high precision.

IV. Conclusion and Discussions

In this paper, we have proposed a FSI multi-channel synchronous rapid ranging system. The multi-channel ranging structure based on dual interferometers is integrated into the system, achieving a more compact design without sacrificing accuracy, which reduces the multi-channel path complexity and ensures the unity of traceability chain for multiple targets. Additionally, the signal mixing method after spectral segmentation effectively suppresses the Doppler error during the optical signal transmission, resulting in a considerable improvement in the efficiency and robustness, without the complex data processing for interference-signal overlap. Based on this scheme, the multi-channel measurement was verified by simulation, and the additional pseudo peaks generated by signal mixing were successfully distinguished according to the FWHM. Then, experiments were subsequently conducted to validate the performance of the system. The ability to suppress Doppler error was evaluated under conditions of harmonic vibration, uniform drift, and stationary targets. The STD before and after compensation demonstrated the system's effective suppression of Doppler error, with a precision of 1 μm achieved when the target was stationary. The multi-channel measurement experiments involving three targets revealed that the use of FWHM could distinguish between real targets and pseudo peaks, and the precision of each target was at a high level. Theoretically, as long as sufficient light intensity is ensured, more target measurements are also feasible, and the channel expansion is easier. Furthermore, there is approximately an inverse relationship between the intensity of light and the number of channels. In this system, the synchronization error of two frequency-tunable lasers could be further reduced in the future. Moreover, further research is needed for the accuracy calibration of different channels. This system would be further integrated and optimized to obtain higher accuracy and stability. Ultimately, the system could be applied to the large-volume non-cooperative measurement tasks, leveraging the potential of multi-channel, non-cooperative target measurement and ADM.

Acknowledgment

The author Qiang Zhou would like to thank Hui Xu for fruitful discussions about the multi-channel targets distinction strategy.

References

[1] J. Tang, C. Emmanouilidis, and K. Salonitis, "Reconfigurable manufacturing systems characteristics in digital twin context," *IFAC-Papers Online*, vol. 53, no. 2, pp. 10585–10590, 2020.
[2] R. Jardim-Goncalves, D. Romero, and A. Grilo, "Factories of the future: Challenges and leading innovations in intelligent manufacturing," *Int. J. Comput. Integr. Manuf.*, vol. 30, no. 1, pp. 4–14, 2017.
[3] Vikas and R. K. Sahu, "A review on application of laser tracker in precision positioning metrology of particle accelerators," *Precis. Eng.*, vol. 71, pp. 232–249, 2021.
[4] J. Wan et al., "Artificial intelligence-driven customized manufacturing factory: Key technologies, applications, and challenges," *Proc. IEEE*, vol. 109, no. 4, pp. 377–398, Apr. 2021.
[5] R. H. Schmitt et al., "Advances in large-scale metrology – review and future trends," *CIRP Ann.*, vol. 65, no. 2, pp. 643–665, 2016.
[6] X. Jia, Z. Liu, Z. Deng, W. Deng, Z. Wang, and Z. Zhen, "Dynamic absolute distance measurement by frequency sweeping interferometry based doppler beat frequency tracking model," *Opt. Commun.*, vol. 430, pp. 163–169, 2019.
[7] J. Zheng et al., "High-precision silicon-integrated frequency-modulated continuous wave LiDAR calibrated using a microresonator," *ACS Photon.*, vol. 9, pp. 2783–2791, 2022.
[8] R. Daendliker et al., "High-accuracy distance measurement with multiple-wavelength interferometry," *Opt. Eng.*, vol. 34, no. 8, pp. 2407–2412, 1995.
[9] C. Li, F. Zhang, and X. Qu, "High-resolution frequency-modulated continuous-wave LiDAR using multiple laser sources simultaneously scanning," *J. Lightw. Technol.*, vol. 41, no. 1, pp. 367–373, Jan. 2023.
[10] Z. Yu, C. Lu, and G. D. Liu, "FMCW LiDAR with an FM nonlinear kernel function for dynamic-distance measurement," *Opt. Exp.*, vol. 30, no. 11, pp. 19582–19596, May 2023.
[11] Renishaw. XM-60 multi-axis calibrator. [Online]. Available: https://www.renishaw.com
[12] Keysight. Optics and laser heads for laser-interferometer positioning systems. [Online]. Available: https://www.keysight.com
[13] B. Hughes, M. Campbell, A. Lewis, G. Lazzarini, and N. Kay, "Development of a high-accuracy multi-sensor, multi-target coordinate metrology system using frequency scanning interferometry and multilateration," *Proc. SPIE*, vol. 10332, 2017, Art. no. 1033202.
[14] K. Wendt, M. Franke, and F. Hrtig, "Measuring large 3D structures using four portable tracking laser interferometers," *Measurement*, vol. 45, no. 10, pp. 2339–2345, 2012.
[15] G. Shi, W. Wang, and F. Zhang, "Precision improvement of frequency-modulated continuous-wave laser ranging system with two auxiliary interferometers," *Opt. Commun.*, vol. 411, no. 1, pp. 152–157, 2018.
[16] Z. Deng, Z. Liu, X. Jia, W. Deng, and X. Zhang, "Dynamic cascade-model-based frequency-scanning interferometry for real-time and rapid absolute optical ranging," *Opt. Exp.*, vol. 27, no. 15, pp. 21929–21945, 2019.
[17] S. Mohammadzadeh et al., "Extreme ultra-wideband optoelectronic frequency-modulated continuous-wave terahertz radar," *Laser Photon. Rev.*, vol. 17, no. 11, 2023, Art. no. 2300396.
[18] H. Wu, F. Zhang, T. Liu, F. Meng, J. Li, and X. Qu, "Absolute distance measurement by chirped pulse interferometry using a femtosecond pulse laser," *Opt. Exp.*, vol. 23, no. 24, pp. 31582–31593, 2015.
[19] S. Zhou, S. Xiong, and G. Wu, "Dual-comb spectroscopy resolved three-degree-of-freedom sensing," *Photon. Res.*, vol. 9, no. 2, pp. 243–251, 2020.

[20] L. Xu, T. F. Wu, J. R. Lin, L. H. Yang, and J. G. Zhu, "Optical frequency comb frequency division multiplexing dispersive interference multi-channel distance measurement," *Nanomanufacturing Metrol.*, vol. 6, 2022, Art. no. 6.
[21] Y. Liu, J. R. Lin, L. H. Yang, Y. L. Wang, and J. G. Zhu, "Construction of traceable absolute distances network for multilateration with a femtosecond pulse laser," *Opt. Exp.*, vol. 26, no. 20, pp. 266618–226632, 2018.
[22] J. Riemensberger et al., "Massively parallel coherent laser ranging using a soliton microcomb," *Nature*, vol. 581, no. 7807, pp. 164–170, 2020.
[23] D. John, H. Ben, A. J. Lancaster, A. J. Lewis, A. J. H. Reichold, and M. S. Warden, "Multi-channel absolute distance measurement system with sub ppm-accuracy and 20 m range using frequency scanning interferometry and gas absorption cells," *Opt. Exp.*, vol. 22, no. 20, pp. 24869–24893, 2014.
[24] C. Lu, G. Liu, B. Liu, F. Chen, and Y. Gan, "Absolute distance measurement system with micron-grade measurement uncertainty and 24 m range using frequency scanning interferometry with compensation of environmental vibration," *Opt. Exp.*, vol. 24, no. 26, pp. 30215–30224, 2016.
[25] Q. Zhou et al., "Efficient method for the compensation of dispersion mismatch in the frequency-scanning interferometry," *Opt. Exp.*, vol. 29, no. 25, pp. 42127–42143, 2021.

Qiang Zhou received the B.S. degree in measuring technology and instruments in 2018 from Tianjin University, Tianjin, China, where he is currently working toward the Ph.D. degree with the State Key Laboratory of Precision Measuring Technology and Instruments. He research interests include length measurement and laser measuring technology.

Tengfei Wu received the Ph.D. degree from Tianjin University, Tianjin, China, in 2013. He is currently an Associate Professor with the State Key Laboratory of Precision Measuring Technology and Instruments, Tianjin University. His current research interests include large scale metrology and laser measuring technology.

Xinyue Long Photograph and biography are not available at the time of publication.

Zhoumo Zeng (Member, IEEE) received the Ph.D. degree from Tianjin University, Tianjin, China, in 1993. He is currently a Professor and the Dean with Precision Instruments and Optoelectronic Engineering School, Tianjin University. He is a member with the China Society of Optics and Optoelectronics Professional Committee, Director with the China Microelectronics Society, and Director with the Tianjin Microcontroller Society.

Jigui Zhu received the M.S. degree from the National University of Defense Technology, Changsha, China, in 1994, and the Ph.D. degree from Tianjin University, Tianjin, China, in 1997. He is currently a Professor with the College of Precision Instrument and Opto-Electronics Engineering, Tianjin University. In April 2016, he was appointed as the Changjiang (Yangtze River) Scholar Distinguished Professor by the Ministry of Education, China. His research interests include laser and optoelectronic measuring technology, large-scale dimensional metrology, and online vision inspection.